

# Interlayer engineering of lattice dynamics and elastic constants of 2D layered nanomaterials under pressure

Received: 9 September 2024

Accepted: 17 May 2025

Published online: 27 May 2025

 Check for updates

Guoshuai Du<sup>1,2,9</sup>, Lili Zhao<sup>3,9</sup>, Shuchang Li<sup>4,9</sup>, Jing Huang<sup>5</sup>, Susu Fang<sup>6</sup>, Wuxiao Han<sup>1,2</sup>, Jiayin Li<sup>1,6</sup>, Yubing Du<sup>1,2</sup>, Jiaxin Ming<sup>1,6</sup>, Tiansong Zhang<sup>1,2</sup>, Jun Zhang<sup>7</sup>, Jun Kang<sup>8</sup>✉, Xiaoyan Li<sup>4</sup>✉, Weigao Xu<sup>3</sup>✉ & Yabin Chen<sup>1,2,8</sup>✉

Interlayer coupling in two-dimensional (2D) layered nanomaterials can provide us strategies to evoke their superior properties, such as the layer-dependent phonon vibration, the formation of moiré excitons and related nontrivial topology. However, to accurately quantify interlayer potential and further measure elastic properties of 2D materials remain challenging, despite significant efforts. Herein, the layer-dependent lattice dynamics and elastic constants of 2D nanomaterials have been systematically investigated via pressure-engineering strategy based on ultralow frequency Raman spectroscopy. The shear and layer-breathing modes Raman shifts of 2H-MoS<sub>2</sub> with various thicknesses are analyzed by the monoatomic chain model (MCM). Intriguingly, it is found that the layer-dependent  $d\omega/dP$  of shear ( $S_{N,1}$ ) and breathing ( $LB_{N,N-1}$ ) modes display the opposite trends, quantitatively consistent with MCM analysis, our molecular dynamics simulations and density functional theory calculations. The diatomic chain model is combined with Raman data to analyze the intralayer and interlayer shear force constants and their pressure coefficients, revealing a strong dependence on the number of layers. These results can be generalized to other van der Waals systems, and may shed light on the potential applications of 2D materials in nanomechanics and nanoelectronics.

The van der Waals interactions between the atomic layers facilitate us to mechanically exfoliate and transfer various two-dimensional (2D) layered nanomaterials, and further to controllably stack their heterostructures<sup>1–7</sup>. Despite its relatively weak characteristic, van der Waals interactions play an essential role in the exotic physical

properties of these quantum systems, such as the layer-dependent phonon vibration, the twist angle-dependent moiré superlattices, the prominent spin-orbital couplings in 2D heavy fermions, and the correlated topological insulators<sup>8–13</sup>. Therefore, the quantitative determination and modulation of interlayer coupling strength in 2D materials

<sup>1</sup>Advanced Research Institute of Multidisciplinary Sciences (ARIMS), Beijing Institute of Technology, Beijing, China. <sup>2</sup>School of Aerospace Engineering, Beijing Institute of Technology, Beijing, China. <sup>3</sup>State Key Laboratory of Coordination Chemistry, Key Laboratory of Mesoscopic Chemistry of MOE, School of Chemistry and Chemical Engineering, Nanjing University, Nanjing, China. <sup>4</sup>Mechano-X Institute, Applied Mechanics Laboratory, Department of Engineering Mechanics, Tsinghua University, Beijing, China. <sup>5</sup>Beijing Computational Science Research Center, Beijing, China. <sup>6</sup>School of Chemistry and Chemical Engineering, Beijing Institute of Technology, Beijing, China. <sup>7</sup>Institute of Semiconductors, Chinese Academy of Sciences, Beijing, China. <sup>8</sup>BIT Chongqing Institute of Microelectronics and Microsystems, Chongqing, China. <sup>9</sup>These authors contributed equally: Guoshuai Du, Lili Zhao, Shuchang Li.

✉ e-mail: [jkang@csrc.ac.cn](mailto:jkang@csrc.ac.cn); [xiaoyanlithu@tsinghua.edu.cn](mailto:xiaoyanlithu@tsinghua.edu.cn); [xuwg@nju.edu.cn](mailto:xuwg@nju.edu.cn); [chyb0422@bit.edu.cn](mailto:chyb0422@bit.edu.cn)

are of significant importance for us to boost their practical applications in twistrionics and optoelectronics. However, it remains a huge challenge. In the previous studies, the interlayer van der Waals interactions in transition metal dichalcogenides have been tentatively quantified according to the pressure-enhanced valance band splitting<sup>14</sup>. Obviously, this approach had material-specific prerequisite, severely relying on the 2D samples displaying the noticeable splitting energy in their valance bands. In addition, the interlayer strength of van der Waals pressure has been measured by trapping pressure-sensitive molecules between graphene layers<sup>15</sup>. Nevertheless, it is important to note that these organic molecules themselves can spontaneously induce the efficient charge transfer and consequently influence the intrinsic interlayer interactions of 2D materials. Moreover, a synchrotron X-ray diffraction experiment has been established to quantify the interlayer interactions in  $\text{TiS}_2$ , and an unexpected accumulation of electron density in the interlayer region was found<sup>10</sup>, which is difficult to popularize due to the limitations of the complex apparatus. Besides, the surface indentation method could measure the perpendicular-to-the-plane elasticity or the adhesion forces between the AFM tip and the supported 2D nanoflake. However, to prevent contamination, the experiment must be carried out in a high vacuum, and the results should be evaluated against benchmarks rather than treated as standalone measurements of adhesion energy or forces<sup>16,17</sup>. In response to these limitations, a strategic approach based on ultralow frequency (ULF) Raman spectroscopy has been developed to quantify the interlayer interactions in multilayer graphene<sup>18</sup>. Such

non-invasive, rapid and convenient technique can be widely extended to numerous 2D materials, and it is suitable for diverse experimental environments as well.

Hydrostatic pressure can effectively modulate the lattice structures and physical properties of 2D nanomaterials, without deliberately introducing any impurities or defects<sup>19</sup>. Extreme pressure can induce interlayer slippage, structural evolutions, metal-insulator transitions, and antiferromagnetic to ferromagnetic transition in 2D materials and heterostructures, owing to their pressure-sensitive interlayer and intralayer interactions<sup>19–22</sup>. Typically, interlayer interactions response more sensitively to pressure than intralayer interactions governed by strong covalent bond. At the same time, the interlayer coupling strength of 2D layered nanomaterial strictly depends on its layer number ( $N$ )<sup>12,23</sup>. For instance, diamond anvil cell (DAC) combined with in-situ synchrotron X-ray diffraction has been utilized to investigate the evolutionary mechanism and stability of bulk  $\text{MoS}_2$  under high pressure, and the obtained equation of state suggested its corresponding bulk modulus of bulk  $\text{MoS}_2$  as  $\sim 79.5$  GPa, while the modulus of ultrathin  $\text{MoS}_2$  remains uncertain<sup>24</sup>. In few-layer  $\text{MoS}_2$ , the interlayer coupling could promote the structural transition from  $2H$  to  $AB'$  configuration of quadlayer  $\text{MoS}_2$  under pressure, as revealed by the high and low frequency Raman vibration<sup>25</sup>. Additionally, the performance of multi-terminal field-effect transistors, employing few-layer  $\text{MoS}_2$  as the channel semiconductor and BN as the dielectric layer, can be notably improved under hydrostatic pressure, accompanied by structural modification<sup>26</sup>. As the thickness reduced to

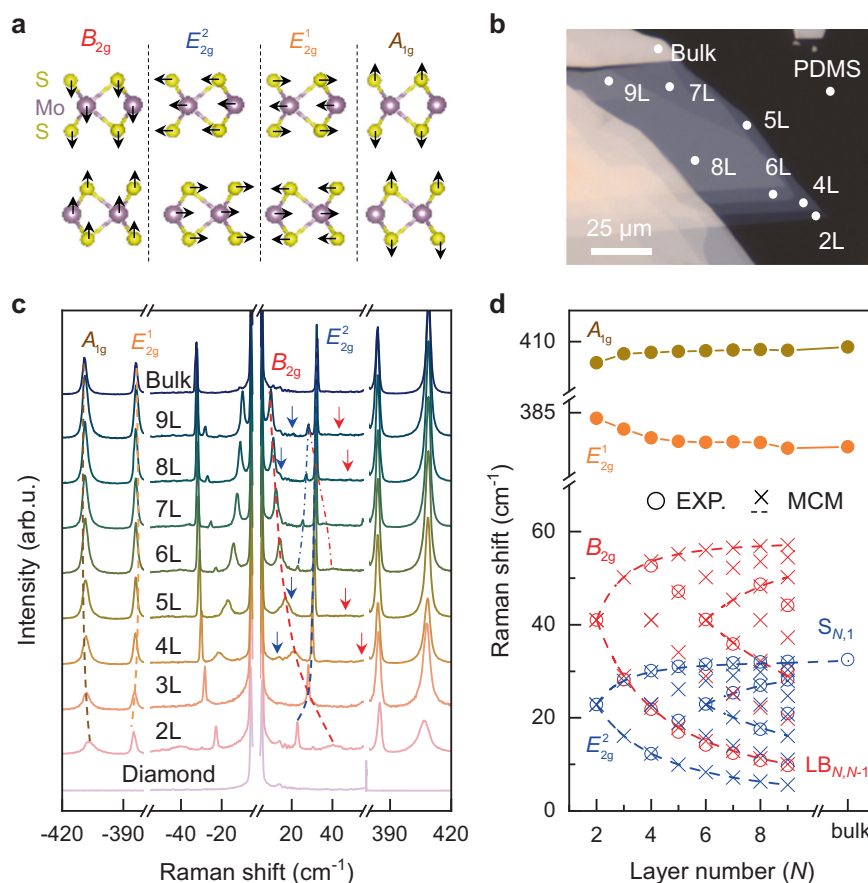


**Fig. 1 | Collective LB and S modes as well as high-frequency intralayer Raman modes of  $2H$ - $\text{MoS}_2$  under ambient pressure. **a** Scheme of Raman-active normal modes of 2D layered  $\text{MoS}_2$ , including the collective LB ( $B_{2g}$ ) and S ( $E_{2g}^2$ ) modes, and intralayer  $E_{2g}^1$  and  $A_{1g}$  modes. **b** Representative optical image of the exfoliated  $\text{MoS}_2$  on a polydimethylsiloxane (PDMS) surface, and the layer numbers of  $\text{MoS}_2$  are labeled. **c** Stokes and anti-Stokes Raman spectra of the few-layer and bulk  $\text{MoS}_2$  on a**

diamond surface. The dashed lines and arrows are used for guide. **d** Raman shifts of few-layer  $\text{MoS}_2$  as a function of  $N$ . The open circles denote the experimental (Exp.) data. The blue (S mode) and red (LB mode) crosses mean the obtained calculation results based on the MCM, and the data on each dashed line are from the same branch. MCM monoatomic chain model, S shear, LB layer breathing.

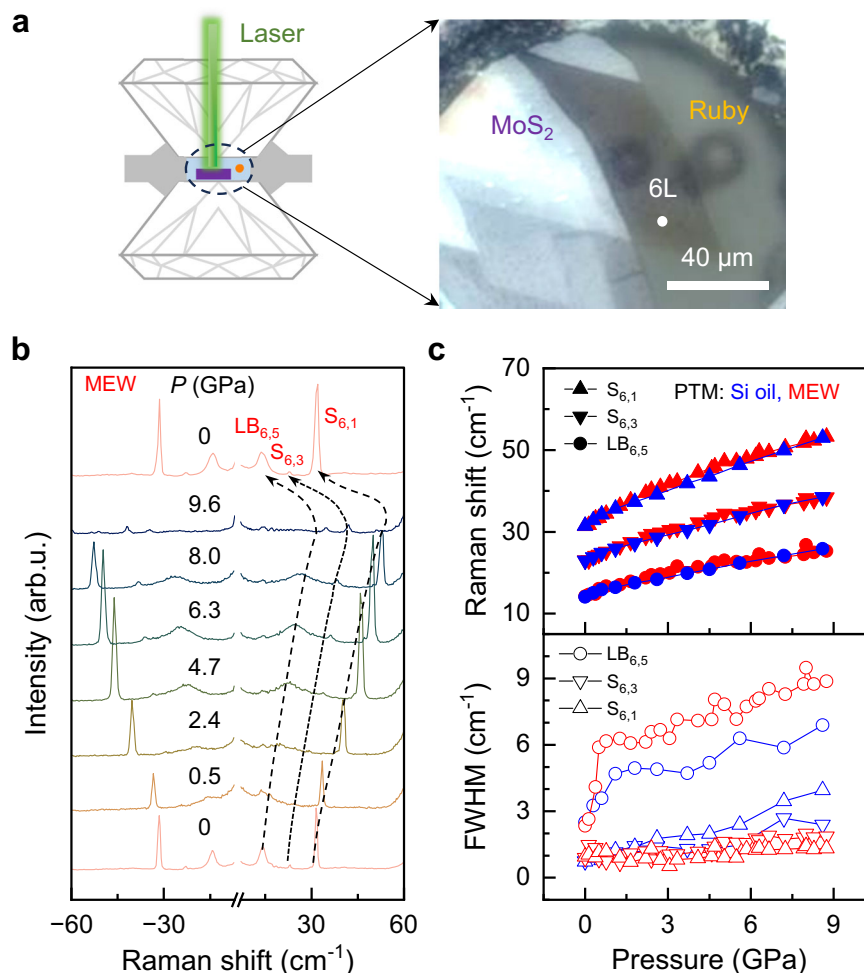


**Fig. 2 | Low-frequency LB and S modes of 6L-MoS<sub>2</sub> under high pressure applied by a DAC. a** 2H-MoS<sub>2</sub> nanoflakes transferred onto diamond surface. The MEW was used as the PTM, and the initial pressure was calibrated as 0.5 GPa. **b** Stokes and anti-Stokes Raman spectra of 6L-MoS<sub>2</sub> under various pressures with MEW as the PTM. The dashed lines indicate the vibrational frequencies of LB<sub>6,5</sub>, S<sub>6,3</sub>, and S<sub>6,1</sub>

modes. **c** Pressure-dependent Raman shifts (upper panel) and FWHM (lower panel) of S<sub>6,1</sub>, S<sub>6,3</sub>, and LB<sub>6,5</sub> modes of 6 L MoS<sub>2</sub> nanoflake with the MEW (red) and silicone oil (blue) media. DAC diamond anvil cell, MEW methanol-ethanol-water, PTM pressure transmitting medium.

monolayer limit, high pressure can principally tune its electronic energies and band structure, such as the transition from direct to indirect band gap<sup>27</sup>. Overall, lattice vibration and structural stability of ultrathin MoS<sub>2</sub> were initially studied under high pressure, implying that both interlayer and intralayer force constants dramatically changed with pressure<sup>25,28–33</sup>. To the best of our knowledge, the comprehensive studies on the pressure-regulated lattice dynamics and elastic constants of MoS<sub>2</sub> with various *N* is still lacking, and the associated mechanism remains unclear.

In this work, pressure engineering approach is developed to systematically investigate the layer-number dependent interlayer interactions in 2D layered materials using in situ ULF Raman spectroscopy, by taking MoS<sub>2</sub> as the typical paradigm. Our experimental results are analyzed with the linear chain model and consistent with the density functional theory (DFT) calculations and molecular dynamics (MD) simulations as well. It is found that force constants and moduli of MoS<sub>2</sub> are dramatically enhanced with pressure, and the evolution of interlayer interactions exhibited a clear layer number (thickness) dependence. More importantly, we find that the monoatomic chain model (MCM) can effectively explain layer dependence of the interlayer and intralayer vibrational pressure coefficients, providing a clear physical model for these pressure coefficients. The results in this study can provide a pivotal reference to clarify the servo response of mechanical properties of 2D materials under extreme pressure.

## Results and discussion

Here we took the commonly studied 2H-MoS<sub>2</sub> (space group *P6<sub>3</sub>/mmc*) with layered structure as a paradigmatic example. In principle, the relevant results can be rationally generalized to a wide family of van der Waals materials and their heterostructures. According to the lattice dynamics theory, each primitive unit cell of MoS<sub>2</sub> consists of two molecules<sup>28</sup>, that is, two Mo atoms and four S atoms. Hence, there exists 18 normal vibrational modes at the Brillouin zone center with the irreducible representations as  $\Gamma = 2A_{2u} \oplus 2E_{1u} \oplus E_{2u} \oplus B_{1u} \oplus A_{1g} \oplus 2B_{2g} \oplus E_{1g} \oplus 2E_{2g}$ , where except for one *A*<sub>2u</sub> and one *E*<sub>1u</sub> acoustic modes, the remained ones originate from the long-wavelength optical phonons<sup>34</sup>. In experiment, three Raman peaks of bulk MoS<sub>2</sub>, i.e., low frequency *E*<sub>2g</sub><sup>2</sup> at 32 cm<sup>-1</sup> and high-frequency *E*<sub>2g</sub><sup>1</sup> (383 cm<sup>-1</sup>) and *A*<sub>1g</sub> (408 cm<sup>-1</sup>), are usually observed without considering the resonance effect<sup>35</sup>. Importantly, the *E*<sub>2g</sub><sup>2</sup> (shear mode (S)), and in-plane *E*<sub>2g</sub><sup>1</sup> and out-of-plane *A*<sub>1g</sub> modes vibrate along the intralayer and interlayer directions, respectively, as shown in Fig. 1a. Notably, the intralayer vibrations refer to the relative motions of atoms within an individual layer, whereas the interlayer vibrations are the collective excitations of the entire MoS<sub>2</sub> layer perpendicular or parallel to the normal direction. More interestingly, these vibrational frequencies are principally sensitive to the *N*<sup>36</sup>. When the thickness of bulk 2H-MoS<sub>2</sub> is shrank to few layer, the point group *D*<sub>6h</sub><sup>4</sup> is changed to *D*<sub>3d</sub> (even number) or *D*<sub>3h</sub> (odd number), as shown in Supplementary Note 1<sup>37</sup>. For even *N*, its layer breathing (LB)

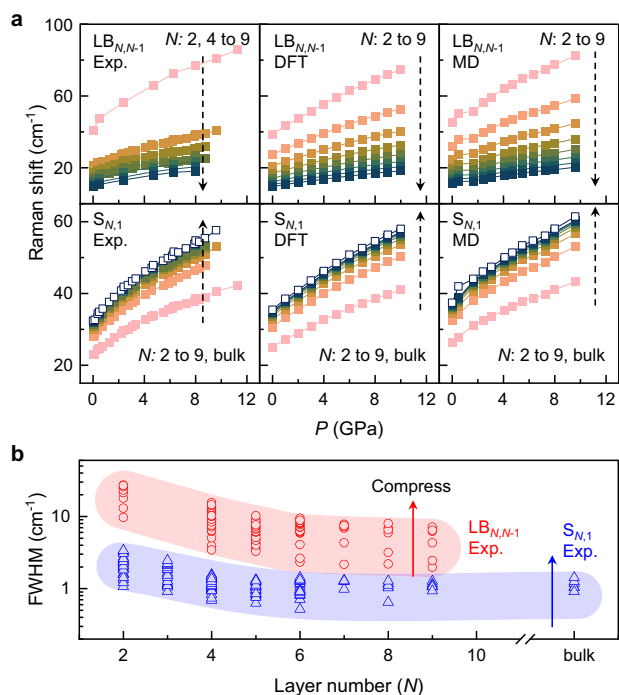


**Fig. 3 | Pressure-dependent Raman results of both LB and S modes of few-layer 2H-MoS<sub>2</sub> (2 to 9 layers) obtained by experiments (Exp.) and theoretical calculations (DFT and MD).** **a** The measured and calculated (DFT and MD) Raman results of LB<sub>*N,N-1*</sub> (upper panel) and S<sub>*N,1*</sub> (lower panel) modes of MoS<sub>2</sub> with different *N*, which cover 2 to 9, and bulk as indicated by dashed lines. **b** The experimental FWHM of LB<sub>*N,N-1*</sub> (red) and S<sub>*N,1*</sub> (blue) modes of MoS<sub>2</sub> with different *N*. Note that the logarithmic scale is used in the y-axis. The red and blue arrows indicate the increasing of pressure. DFT density functional theory, MD molecular dynamics.

and S modes are classified as either Raman-active or IR-active; for odd *N*, the LB modes can be either Raman-active or IR-active, while the S modes can be Raman-active or both Raman-active and IR-active. In normal, *N*-layer MoS<sub>2</sub> typically includes (*N*-1) two-fold degenerated S modes and (*N*-1) nondegenerate LB modes, as shown in Supplementary Fig. 1 and 2. Supplementary Fig. 3 to 7 show S<sub>*N,1*</sub> and LB<sub>*N,N-1*</sub> vibrational modes of 2 L to 6 L 2H-MoS<sub>2</sub> under ambient pressure from MD simulations, respectively. By analyzing the amplitudes in time domain and frequency domain, along with the corresponding phases, we can assign the specific phonon mode for a given vibrational frequency.

Figure 1b displays the representative few-layer MoS<sub>2</sub> nanoflake exfoliated from the high-quality bulk crystal, with the thickness exactly determined by the combined optical contrasts and low-frequency Raman spectra. Figure 1c presents the detailed Stokes and anti-Stokes Raman spectra of MoS<sub>2</sub> nanoflake with various *N*, acquired using our homemade Raman system with its layout shown in Supplementary Fig. 8. The extracted *N*-dependent Raman shifts are summarized in Fig. 1d. As *N* increases, the high-frequency E<sub>2g</sub><sup>1</sup> and A<sub>1g</sub> modes shift oppositely till saturation when *N* exceeds around 5, well consistent with the literature<sup>35</sup>.

Next, for the low-frequency E<sub>2g</sub><sup>2</sup> and B<sub>2g</sub> modes, the MCM can be used to explain the experimental results, when considering that each individual layer rigidly vibrates against its adjacent layer. In this scenario, each MoS<sub>2</sub> layer can be simplified as a rigid ball with the mass density  $\mu$  (the total mass per unit area), and interlayer interactions can be represented by the elastic constant  $\alpha$  between balls. Therefore, by diagonalizing the  $N \times N$  dynamical matrix, the frequencies of (*N*-1) two-fold degenerate S modes and (*N*-1) LB modes can be calculated as  $\omega(S_{N,N-j}) = \omega(S_{\text{bulk}}) \sin(j\pi/2N)$ , and  $\omega(\text{LB}_{N,N-j}) = \omega(\text{LB}_{\text{bulk}}) \sin(j\pi/2N)$ , respectively<sup>37</sup>, where the  $\omega(S_{\text{bulk}}) = 1/\pi c \sqrt{\alpha^{\parallel}/\mu}$  and  $\omega(\text{LB}_{\text{bulk}}) = 1/\pi c \sqrt{\alpha^{\perp}/\mu}$  are attributed

from the S and LB modes of bulk crystals and  $j = 1, 2, 3, \dots, N-1$ .  $\alpha^{\parallel}$  ( $\alpha^{\perp}$ ) corresponds to the in-plane (out-of-plane) interlayer force constant per unit area between the nearest-neighbors,  $\mu$  is the total mass per unit area of each layer, and  $c$  is the speed of light. Obviously, S<sub>*N,N-1*</sub>/LB<sub>*N,N-1*</sub> with  $j = N-1$  is the highest-frequency branch, while S<sub>*N,N-1*</sub>/LB<sub>*N,N-1*</sub> ( $j = 1$ ) means the lowest-frequency branch. As shown in Fig. 1d, our experimental data can be well fitted with the MCM, implying the negligible coupling of MoS<sub>2</sub> layer with its substrate. Besides, the third highest-frequency S<sub>*N,3*</sub> mode together with the lowest-frequency LB<sub>*N,N-1*</sub> and the third lowest-frequency LB<sub>*N,N-3*</sub> modes of few layer MoS<sub>2</sub> have been observed in Raman spectra as well, despite their weak intensities<sup>38</sup>. The  $\alpha^{\parallel}$  and  $\alpha^{\perp}$  for 2H-MoS<sub>2</sub> under ambient condition were derived as  $2.8 \times 10^{19}$  and  $8.6 \times 10^{19} \text{ N m}^{-3}$ , respectively, which is quantitatively consistent with those in the literature<sup>38</sup>. Furthermore, we performed the detailed DFT calculations and MD simulations to gain more insights on the *N*-dependence of vibrational frequency of MoS<sub>2</sub>, and the results were in good agreement with the experimental data, as illustrated in Supplementary Fig. 9.

To probe the pressure effect on the interlayer and intralayer couplings of MoS<sub>2</sub>, we transferred the few-layer MoS<sub>2</sub> onto the diamond culet and the extreme hydrostatic pressure can be generated with a symmetrical DAC, as shown in Fig. 2a. Such a GPa-level pressure can conveniently shorten both the interlayer and intralayer distances, and thus effectively modulate the relevant Raman frequencies. Figure 2b exhibits the evolution of Raman spectra of 6 L MoS<sub>2</sub> under high pressure up to 9.6 GPa with the mixture of methanol-ethanol-water (MEW, 16:3:1) used as the pressure transmitting medium (PTM), and the structural transitions may happen at such high pressure<sup>25</sup>. From our MD simulations, four low-frequency Raman modes as S<sub>6,1</sub>, S<sub>6,3</sub>, LB<sub>6,3</sub> and LB<sub>6,5</sub> can be detected under ambient pressure (Supplementary Fig. 10), as discussed previously in Fig. 1c. When subjected to high pressure, the LB<sub>6,3</sub> mode weakened dramatically and became undetectable in our experiments (Fig. 2b and Supplementary Fig. 11). The intensity of three remained modes gradually decreased as the pressure increased, primarily owing to the phonon scattering with the surrounding transmitting medium or the enriched charge carriers. Under high pressure, all Raman frequencies of S<sub>6,1</sub>, S<sub>6,3</sub>, and LB<sub>6,5</sub> exhibit the significant blue-shift, which can be well explained by the compressed lattice constants and resultant enhanced lattice structure of MoS<sub>2</sub> under pressure. When the pressure totally released, the Raman vibrations basically return to the initial state, as shown in Fig. 2b. Typically, the lattice constant  $c$  is reduced by 6.4% at -10 GPa<sup>24</sup>. Impressively, the S modes strengthened more rapidly with a larger slope  $d\omega/dP$  than LB mode in Fig. 2c. In general, LB modes involve the out-of-plane atomic motions and should therefore be more sensitive to the variation of interlayer spacing than S modes. However, the intuitive analysis is indeed inconsistent with our experimental data in Fig. 2c. Below, we will make the detailed discussion on this unexpected phenomenon. On the other hand, the full width at half-maximum (FWHM) of each peak became larger under high pressure, and the LB mode presents more prominent, indicating its shorter lifetime  $\tau$ , due to the anharmonic decay of phonon transport. For instance, the FWHM of LB<sub>6,5</sub> mode was enlarged from -2.3 (0 GPa) to 9.5 cm<sup>-1</sup> (8 GPa), resulting in the reduced  $\tau$  from 14.3 to 3.5 ps based on the uncertainty principle  $\Delta E \sim \hbar/\tau$ .

In addition, when PTM was replaced with silicone oil, blue shift trend of low frequency Raman vibration of MoS<sub>2</sub> is qualitatively consistent with those by MEW, as shown in Fig. 2c. Notably, the FWHM of S vibration widens more significantly than that in MEW, while the increase of FWHM in LB vibration is smaller than that in MEW. This phenomenon indicates that MEW offers good hydrostatic performance in the current pressure range ( $P < 10 \text{ GPa}$ )<sup>39</sup>, producing negligible shear stress on MoS<sub>2</sub> sample, which leads to widened FWHM for S modes. Therefore, the significant widening of FWHM for LB vibration in MEW is mainly due to the effect of hydrostatic pressure.

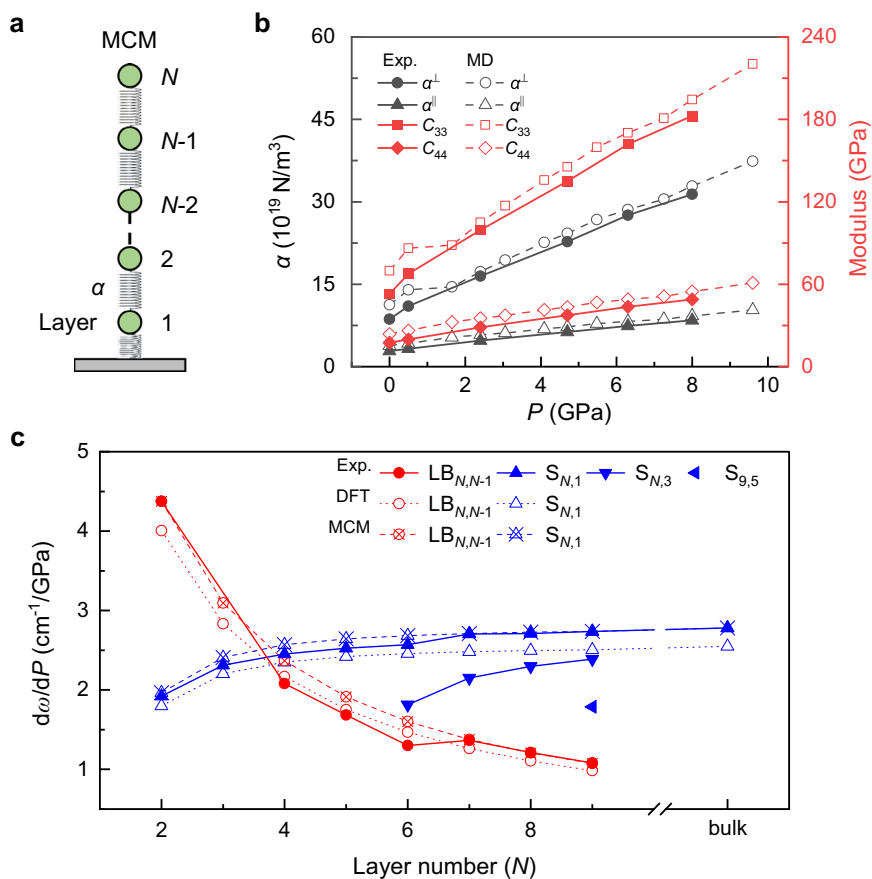


**Fig. 4 | Pressure-modulated elastic constants and lattice dynamics of few-layer 2H-MoS<sub>2</sub>.** **a** MCM of MoS<sub>2</sub> on a solid substrate. **b** Evolution of force constants ( $\alpha^{\perp}$  and  $\alpha^{\parallel}$ ) and moduli ( $C_{33}$  and  $C_{44}$ ) of LB and S modes of MoS<sub>2</sub> under high pressure. The solid and empty symbols denote the exp. and MD results, respectively. The changes in the force constant and modulus under high pressure seem linear,

leading to the nonlinear dependence of Raman scattering on pressure. **c**  $N$ -dependence of Raman shifting rates of  $d\omega(\text{LB})/dP$  and  $d\omega(\text{S})/dP$  of MoS<sub>2</sub>. Note that  $d\omega(\text{LB})/dP$  and  $d\omega(\text{S})/dP$  intersect when  $N$  approaches to  $-4$ . The solid, empty, and empty with X intersection symbols denote the exp., DFT, and MCM results, respectively. The dashed and solid lines are guides for the eyes.

To investigate the  $N$ -dependence of low-frequency Raman shifts of 2H-MoS<sub>2</sub> under high pressure, we measured the Raman spectra of MoS<sub>2</sub> nanoflakes with different  $N$  in DAC. The acquired Raman results of the lowest-frequency LB <sub>$N,N-1$</sub>  and the highest-frequency S <sub>$N,1$</sub>  modes are displayed in Fig. 3a, as well as the DFT and MD calculations. Apparently, for a MoS<sub>2</sub> nanoflake with the given  $N$ , both LB <sub>$N,N-1$</sub>  and S <sub>$N,1$</sub>  modes monotonically display the evidently blueshifted vibrational energies (Fig. 3a) and the broadened linewidths (Fig. 3b) with pressure, similar with the results of 6L-MoS<sub>2</sub> in Fig. 2. Interestingly, LB and S modes present distinct Raman shift rates with pressure, that is,  $d\omega(\text{LB}_{N,N-1})/dP$  ( $d\omega(\text{S}_{N,1})/dP$ ) becomes smaller (larger) as the  $N$  increases. These exotic results were further confirmed by the theoretical calculations using both DFT and MD approaches (Fig. 3a). The quantitative analysis will be discussed later in Fig. 4. The Raman vibrations of bilayer MoS<sub>2</sub> still remained observable when the pressure exceeds 9.6 GPa, instead of the total vanishing in methanol-ethanol-water mixture, as shown in Supplementary Figs 12–16. Furthermore, the FWHM of LB <sub>$N,N-1$</sub>  mode was superior to that of S <sub>$N,1$</sub>  mode, and both of them decreased with  $N$ , as shown in Fig. 3b, which is rather consistent with the literature results<sup>36,40</sup>. As the applied pressure increases, for a given  $N$  of MoS<sub>2</sub>, the FWHM values of LB modes became remarkably widened, due to the reduced phonon lifetime caused by pressure. The layer-dependent broadening of FWHM under high pressure is discussed in more detail in Supplementary Fig. 17.

To better understand pressure effect on the interlayer interactions of MoS<sub>2</sub>, we utilized MCM to thoroughly analyze the

low-frequency Raman modes of  $N$ -layer MoS<sub>2</sub> under various pressures as shown in Fig. 4a and Supplementary Fig. 18, which allowed us to evaluate the S ( $\alpha^{\parallel}$ ) and LB ( $\alpha^{\perp}$ ) force constants, as well as the S modulus ( $C_{44}$ ) and LB modulus ( $C_{33}$ ). In terms of nanomechanics, we understand that  $C_{33} = \alpha^{\perp}t$  and  $C_{44} = \alpha^{\parallel}t$ , where  $t$  corresponds to the equilibrium distance between the neighboring layers of MoS<sub>2</sub> under the specific pressure condition<sup>18,24</sup>. As shown in Fig. 4b, the elastic constant  $\alpha^{\parallel}$  of S mode dramatically increased from  $2.8 \times 10^{19}$  (0 GPa) to  $8.4 \times 10^{19}$  (8 GPa)  $\text{N m}^{-3}$ . In contrast, the  $\alpha^{\perp}$  of LB mode responds more quickly on pressure from  $8.6 \times 10^{19} \text{ N m}^{-3}$  at 0 GPa to  $31.4 \times 10^{19} \text{ N m}^{-3}$  at 8 GPa, owing to the more significant compression of interlayer distance ( $\beta_c = 10.4 \times 10^{-3}/\text{GPa}$ ,  $\beta_a = 2.6 \times 10^{-3}/\text{GPa}$ )<sup>24</sup> under pressure. The derived  $C_{33}$  and  $C_{44}$  moduli presents similar behavior after calibrating the thickness of MoS<sub>2</sub> under pressure, which is consistent with our MD calculations and literature results<sup>41</sup>. The obtained force constants by fitting through MCM theory are consistent with those calculated from MD simulations, and the MD-derived force constants are based on the bulk MoS<sub>2</sub> under hydrostatic pressure. This indicates that the few-layer and bulk samples should be in the similar stress environment. Additionally, during decompression process, Raman spectra of 2H-MoS<sub>2</sub> exhibited good recovery in Supplementary Fig. 19.

We further summarized all the  $d\omega/dP$  data of LB and S modes for MoS<sub>2</sub> with different  $N$ , obtained by experiments and DFT calculations, as shown in Fig. 4c. It is clear that as  $N$  increased,  $d\omega(\text{S}_{N,1})/dP$

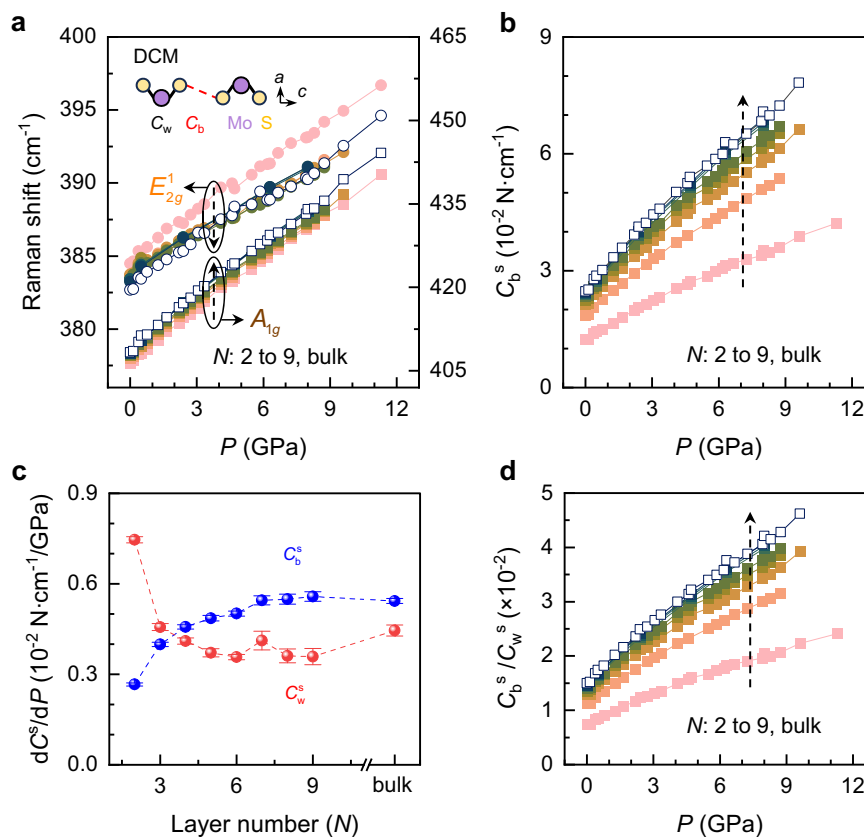


**Fig. 5 | DCM used to analyze the high-frequency Raman vibrations and elastic constants of 2H-MoS<sub>2</sub> under high pressure.** **a** High-frequency Raman modes  $A_{1g}$  and  $E_{2g}^1$  of MoS<sub>2</sub> with various  $N$ , and  $N$  changed from 2 to 9, and bulk. Inset shows the DCM of MoS<sub>2</sub>. **b** Pressure-dependence of shear force constant  $C_b^s$  between the chalcogen planes of the neighboring layers with various  $N$ . **c** The extracted  $dC_w^s/dP$

and  $dC_b^s/dP$  slopes of MoS<sub>2</sub> as a function of  $N$  under pressure. The  $C_w^s$  is the shear constant between Mo and S atomic planes in an individual layer. The error bars represent the standard deviation obtained from linear fitting. **d** The obtained  $C_b^s/C_w^s$  of MoS<sub>2</sub> with different  $N$ . DCM diatomic chain model.

gradually increased and then became saturated at about 6 layers, while  $d\omega(LB_{N,N-1})/dP$  conversely decreased and became saturated at  $\sim 9$  layers. Moreover, when the  $N$  was less than 4, the  $d\omega(LB_{N,N-1})/dP$  values were obviously larger than  $d\omega(S_{N,1})/dP$ , however, the results are reversed when  $N \geq 4$ . This can be well explained by the MCM, as shown in Fig. 4c. For the  $S_{N,1}$  mode, we know  $d\omega(S_{N,1})/dP = [d\omega(S_{bulk})/dP] \sin[\pi(N-1)/2N]$ . Since  $d\omega(S_{bulk})/dP$  is kept as a constant,  $d\omega(S_{N,1})/dP$  monotonically increases as the  $N$ . Breathing mode  $LB_{N,N-1}$  has the similar result,  $d\omega(LB_{N,N-1})/dP = [d\omega(LB_{bulk})/dP] \sin(\pi/2N)$ , and thus  $d\omega(LB_{N,N-1})/dP$  decreases as  $N$  increases. Moreover,  $C_{33}$  is more sensitive to pressure than  $C_{44}$ , leading to  $d\omega(LB_{bulk})/dP > d\omega(S_{bulk})/dP$ . When  $N=2$ ,  $d\omega(S_{2,1})/dP < d\omega(LB_{2,1})/dP$  can be decided. When  $N$  approaches the infinity,  $d\omega(LB_{N,N-1})/dP \rightarrow 0 < d\omega(S_{N,1})/dP - d\omega(S_{bulk})/dP$ . So there must be a crossover between  $d\omega(S_{N,1})/dP$  and  $d\omega(LB_{N,N-1})/dP$  at a finite  $N$ , well consistent with our experimental results in Fig. 4c. Alternatively, this phenomenon might be understood by different stress states of MoS<sub>2</sub> nanoflakes with different  $N$  as well<sup>42</sup>. For the ultrathin MoS<sub>2</sub> ( $N=2$ ), it mostly endures the uniaxial compression. For the thicker and bulk MoS<sub>2</sub>, hydrostatic pressure dominates Raman responses of MoS<sub>2</sub> over stress conditions.

To further investigate this phenomenon, we compared the pressure responses of MoS<sub>2</sub> with different  $N$  in two PTMs: silicone oil (Supplementary Fig. 20) and MEW. As shown in Supplementary Fig. 21, the MCM theory can accurately predict the  $d\omega/dP$  variation for low-frequency Raman modes of MoS<sub>2</sub> in both cases. In the silicone oil with inferior hydrostaticity<sup>39</sup>, the obtained  $d\omega/dP$  is generally lower than that in MEW with better hydrostatic pressure. This indicates that few-

layer MoS<sub>2</sub> has stress states similar to those of bulk samples, otherwise, the MCM theory may become invalid. Given the strong correlation between the experimental and simulation results, it is believed that MoS<sub>2</sub> samples endure hydrostatic pressure environment when using MEW medium, regardless of its layer number. Furthermore, we found that the MCM theory is applicable to 3R-MoS<sub>2</sub> (Supplementary Fig. 22) and the previously reported 2H-MoTe<sub>2</sub><sup>12</sup> (Supplementary Fig. 23) as well. However, for bilayer MoS<sub>2</sub> with a twist angle ( $\sim 10 \pm 0.6^\circ$ ), the high-pressure Raman response dramatically differs from that of naturally stacked bilayer MoS<sub>2</sub>, due to phonon renormalization effect (Supplementary Fig. 24).

In order to further elaborate the influence of external pressure on elastic constants of MoS<sub>2</sub>, diatomic chain model (DCM) theory proposed by Wieting<sup>28,43</sup>, which considers both intralayer and interlayer interactions, was adopted to analyze our experimental data, as shown in Fig. 5a. In this model (inset of Fig. 5a), the shear and compressive force constants between the chalcogen planes of the neighboring layers are defined as  $C_b^s$  and  $C_w^s$ , and between the molybdenum and chalcogen planes in a layer are  $C_w^s$  and  $C_b^s$ , respectively. Based on Raman results of the in-plane  $E_{2g}^1$  and  $E_{2g}^2$  in Figs. 5a, 3a and Supplementary Note 2 in Supplementary Information, the values of  $C_w^s$  and  $C_b^s$  under each pressure can be deduced readily, as shown in Fig. 5b and Supplementary Fig. 25. The values of  $C_b^s$  rapidly increased with pressure, among which bilayer MoS<sub>2</sub> changes the slowest as shown in Fig. 5b, and the change rate increases gradually with the increase of  $N$  in Fig. 5c. It is obvious that the slope values become saturated as  $N$  increases to 6, quantitatively consistent with the results of MCM mentioned above in Fig. 4c. Similarly, the slope change of  $C_w^s$  has the

comparable trend with that of  $C_b^s$ . The linear slope  $dC_b^s/dP$  of  $N=2$  and bulk  $\text{MoS}_2$  were calculated as  $0.27 \times 10^{-2}$  and  $0.58 \times 10^{-2} \text{ cm}^{-1}/\text{GPa}$ , respectively. In addition, the ratio of  $C_b^s/C_w^s$  indicates the relative strength of interlayer and intralayer interactions, and thus the greater the ratio, the stronger the interlayer coupling. Figure 5d shows the calculated  $C_b^s/C_w^s$  data of  $\text{MoS}_2$  with different  $N$ . With the increase of the  $N$ , the  $C_b^s/C_w^s$  ratio became larger, indicating that the interlayer interactions and the  $N$  displayed the basically positive correlation. The value of  $C_b^s/C_w^s$  gradually increases with pressure, but it remained less than 4.5% under -8 GPa, indicating that the  $NL$   $\text{MoS}_2$  still retained the acceptable 2D characteristic even under such high pressure.

In conclusion, we systematically investigated the interlayer and intralayer interactions of 2D layered  $\text{MoS}_2$  under extreme pressure by the ULF Raman spectroscopy, together with DFT calculations and MD simulations. The obtained  $N$ -dependent Raman results were analyzed through the MCM and DCM. Both interlayer and intralayer force constants gradually increased as pressure increased, with a more significant increment in the interlayer coupling owing to its rapid pressure response. Furthermore, it was found that the shift rates of  $\text{LB}_{N,N-1}$  modes gradually decreased as  $N$  became larger, dramatically different from the  $\text{S}_{N,1}$  modes, which can be explained using the MCM model under high pressure. Additionally, the MCM model could be used to predict the low-frequency Raman vibrational response of various naturally stacked 2D materials under high pressure, not just  $2H$ - $\text{MoS}_2$ . The current study is expected to offer insights into pressure-engineering of physical properties of 2D materials and further promote their potential applications in nanomechanics and optoelectronics.

## Methods

### Preparation of $\text{MoS}_2$ nanoflakes and the characterizations

Few-layer  $\text{MoS}_2$  nanoflakes were prepared by mechanical exfoliation from the commercial  $\text{MoS}_2$  crystals with high quality (2D Semiconductors, USA). Polydimethylsiloxane was utilized as the template, instead of the conventional Scotch tape to exclusive any tape residual, and then  $\text{MoS}_2$  nanoflakes were directly transferred onto the culet of diamond. The entire dry-transfer process can guarantee the clean  $\text{MoS}_2$  surface without any contamination or dirt. Layer number of few-layer  $\text{MoS}_2$  nanoflakes was exactly determined by combining optical contrast and low-frequency Raman spectra.

### High-pressure raman spectroscopy

We used a symmetric DAC with a  $\sim 400 \mu\text{m}$  culet to generate high pressure on  $\text{MoS}_2$  nanoflakes. A T301 gasket with the central  $\sim 160 \mu\text{m}$  hole drilled by laser milling was used as the sample chamber. The pressure was calibrated by the shifted fluorescence peak of the tiny ruby ball, placed near to the  $\text{MoS}_2$  nanoflakes in DAC. The methanol-ethanol-water (16:3:1) mixture was used as pressure transmitting medium, in order to compare the hydrostatic pressure effect on Raman spectra of  $\text{MoS}_2$ .

All Raman spectrum were acquired through our homemade Raman system, which is based on the SmartRaman confocal-micro-Raman module (Institute of Semiconductors, Chinese Academy of Sciences) and equipped with the Horiba iHR550 spectrometer and 532 nm laser as an excitation source. Importantly, the laser power was optimized to be low enough, in order to avoid the possible overheating effect. A single-longitudinal-mode laser with narrow linewidth and high stability (MSL-III-532), and a narrow linewidth (better than  $10 \text{ cm}^{-1}$ ) bandpass filter (BPF) based on the volume Bragg grating (VBG) technique was used to detect the low-frequency Raman modes<sup>37</sup>. Three VBG-based notch filters (BNF) (bandwidth:  $\sim 8$ – $10 \text{ cm}^{-1}$ ) with high transmittance (up to 80%–90% dependent on the laser wavelength) and an optical density (OD) 3–4 were strategically used to suppress the strong Rayleigh background, and the BPF was utilized to remove any plasma line of laser source. Moreover, two mirrors behind the

reflecting filter (BPF) were used to align the laser beam to the center of the first BNF, as shown in Supplementary Fig. 8. The angles of three BNFs were precisely tuned to block the Rayleigh line up to  $10^{-9}$ – $10^{-12}$ . An iHR550 spectrometer was equipped to detect the Raman scattering signals.

### DFT calculations

DFT calculations were performed by the Vienna Ab initio Simulation Package<sup>44,45</sup>. The projector-augmented wave method<sup>46</sup> was adopted to describe the core-valence interaction. The exchange-functional was treated by the generalized gradient approximation of the Perdew-Burke-Ernzerhof functional<sup>47</sup>. The energy cut-off for the plane wave basis expansion was set to 500 eV and the convergence criterion of geometry relaxation was set to 5 meV/Å. The self-consistent calculations applied a convergence energy threshold of  $10^{-5}$  eV. A  $12 \times 12 \times 1$  Monkhorst-Pack  $k$ -point grid<sup>48</sup> was used to sample the Brillouin zone of the unit cell of bulk  $\text{MoS}_2$ . The van der Waals interaction was included through Grimmes's DFT-D3 method<sup>49</sup>. The phonon modes were calculated using the finite displacement method.

### MD simulations

To evaluate the dynamic characteristics of multi-layer  $\text{MoS}_2$ , we performed a series of large-scale MD simulations for the vibrations of multi-layer  $\text{MoS}_2$  under different pressures. All MD simulations were performed via the large-scale atomic/molecular massively parallel simulator (LAMMPS)<sup>50</sup>. We constructed 2- to 6-layer  $2H$ - $\text{MoS}_2$  samples with the same in-plane dimensions of  $10.52 \times 9.91 \text{ nm}^2$  and an interlayer spacing of 0.62 nm. During simulations, we used the reactive empirical bond-order (REBO) potential<sup>51</sup> and registry-dependent interlayer potential (ILP)<sup>52,53</sup> to describe the bonded intralayer and non-bonded interlayer interactions of Mo and S atoms, respectively. The REBO potential can accurately describe the thermodynamic, structural, and mechanical properties of single-layer  $\text{MoS}_2$ <sup>51</sup>. The ILP incorporates the long-range vdW attraction and the short-range Pauli repulsion between two layers of multi-layer  $\text{MoS}_2$  system<sup>52,53</sup>. Since the ILP is benchmarked against DFT calculations and is augmented by a nonlocal many-body dispersion treatment of long-range correlation, this potential can effectively capture the physical and mechanical properties of polarizable multi-layer  $\text{MoS}_2$  systems<sup>52,53</sup>.

We first performed MD simulations to investigate the vibration modes of 2- to 6-layer  $2H$ - $\text{MoS}_2$  under 0 GPa. All simulated samples were equilibrated by initial energy minimization and subsequent free relaxation for 250 ps. During free relaxation, the pressures were controlled as zero, and the temperature was kept at 300 K via an isothermal-isobaric ensemble<sup>54</sup>. Periodic boundary conditions were imposed along two in-plane directions, while free boundary condition was applied along the out-of-plane direction. After free relaxation, we monitored the centroid coordinates of each  $\text{MoS}_2$  layer at an interval of 1 fs for 50 ps, and obtained the evolution curve of vibration displacement of each layer with time. Then, we performed fast Fourier transform (FFT) on the vibration displacement-time curves to make the spectrum and modal analyzes on the variation of simulated samples. Furthermore, we performed MD simulations to further investigate the vibration modes of bulk  $2H$ - $\text{MoS}_2$  under different pressures. We constructed the  $2H$ - $\text{MoS}_2$  bulk by applying periodic boundary conditions along all three directions of a 6-layer  $2H$ - $\text{MoS}_2$  throughout simulations. The sample was equilibrated by initial energy minimization and subsequent free relaxation at 300 K for 100 ps. After equilibration, the hydrostatic pressure was controlled to reach the target values (0, 0.5, 1.7, 2.4, 3.1, 4.1, 4.7, 5.5, 6.3, 7.3, 8.0, and 9.6 GPa). The simulated sample was relaxed for 250 ps under a given pressure. Both pressure and temperature were controlled using an isothermal-isobaric ensemble<sup>54</sup>. We obtained the time-evolution curve of vibration displacement for each layer by monitoring the variation of centroid coordinate of each layer with time,

and then performed spectrum and modal analyses on these time-evolution curves via FFT. Subsequently, we calculated the vibration frequencies ( $\omega(S_{\text{bulk}})$  and  $\omega(LB_{\text{bulk}})$ ) and the interlayer force constants ( $\alpha_0^\perp$  and  $\alpha_0^\parallel$ ) per unit area of bulk sample by plugging the highest frequencies of S and LB modes obtained from MD simulations into the MCM. Then, we obtained the variation of the frequencies ( $\omega(S_{N,i})$  and  $\omega(LB_{N,i})$ ) with the layer number  $N$  by substituting the vibration frequencies ( $\omega(S_{\text{bulk}})$  and  $\omega(LB_{\text{bulk}})$ ) of S and LB modes of bulk sample into the MCM. Using the conversion relationship between the frequency and the Raman shift, we can determine the dependence of the Raman shift of multi-layer 2H-MoS<sub>2</sub> on the layer numbers.

## Data availability

The source data presented in this study have been deposited in the figshare database under access code <https://doi.org/10.6084/m9.figshare.28815164.v2>. All raw data generated during the current study are available from the corresponding authors upon request. Source data are provided with this paper.

## References

- Satterthwaite, P. F. et al. Van der Waals device integration beyond the limits of van der Waals forces using adhesive matrix transfer. *Nat. Electron.* **7**, 17–28 (2024).
- Manzeli, S., Ovchinnikov, D., Pasquier, D., Yazyev, O. V. & Kis, A. 2D transition metal dichalcogenides. *Nat. Rev. Mater.* **2**, 17033 (2017).
- Fiori, G. et al. Electronics based on two-dimensional materials. *Nat. Nanotechnol.* **9**, 768–779 (2014).
- Butler, S. Z. et al. Progress, challenges, and opportunities in two-dimensional materials beyond graphene. *ACS Nano* **7**, 2898–2926 (2013).
- Kim, J.-y, Ju, X., Ang, K.-W. & Chi, D. Van der Waals layer transfer of 2D materials for monolithic 3D electronic System integration: review and outlook. *ACS Nano* **17**, 1831–1844 (2023).
- Xu, W. et al. Correlated fluorescence blinking in two-dimensional semiconductor heterostructures. *Nature* **541**, 62–67 (2017).
- Li, H. et al. Spontaneous polarity flipping in a 2D heterobilayer induced by fluctuating interfacial carrier flows. *Nano Lett.* **21**, 6773–6780 (2021).
- Wang, H. et al. Planar hyperbolic polaritons in 2D van der Waals materials. *Nat. Commun.* **15**, 69 (2024).
- Eliel, G. S. N. et al. Intralayer and interlayer electron–phonon interactions in twisted graphene heterostructures. *Nat. Commun.* **9**, 1221 (2018).
- Qiu, X. & Ji, W. Illuminating interlayer interactions. *Nat. Mater.* **17**, 211–213 (2018).
- Posey, V. A. et al. Two-dimensional heavy fermions in the van der Waals metal CeSi<sub>3</sub>. *Nature* **625**, 483–488 (2024).
- Xie, X. et al. Unveiling layer-dependent interlayer coupling and vibrational properties in MoTe<sub>2</sub> under high pressure. *Phys. Rev. B* **108**, 155302 (2023).
- Fang, S. et al. Direct characterization of shear phonons in layered materials by mechano-Raman spectroscopy. *Nat. Photonics* **17**, 531–537 (2023).
- Ci, P. et al. Quantifying van der Waals interactions in layered transition metal dichalcogenides from pressure-enhanced valence band splitting. *Nano Lett.* **17**, 4982–4988 (2017).
- Vasu, K. S. et al. Van der Waals pressure and its effect on trapped interlayer molecules. *Nat. Commun.* **7**, 12168 (2016).
- Sun, Y., Sun, Y., Wang, R. & Liu, K. Probing the interlayer mechanical coupling of 2D layered materials - A review. *Prog. Nat. Sci. Mater. Int.* **32**, 528–537 (2022).
- Li, B. et al. Probing van der Waals interactions at two-dimensional heterointerfaces. *Nat. Nanotechnol.* **14**, 567–572 (2019).
- Tan, P. H. et al. The shear mode of multilayer graphene. *Nat. Mater.* **11**, 294–300 (2012).
- Zhang, L. et al. 2D materials and heterostructures at extreme pressure. *Adv. Sci.* **7**, 2002697 (2020).
- Pei, S., Wang, Z. & Xia, J. High pressure studies of 2D materials and heterostructures: a review. *Mater. Des.* **213**, 110363 (2022).
- Han, W. et al. Pressure-modulated structural and magnetic phase transitions in two-dimensional FeTe: tetragonal and hexagonal polymorphs. *Nano Lett.* **24**, 966–974 (2024).
- Du, G. et al. Thermodynamic origins of structural metastability in two-dimensional black arsenic. *J. Phys. Chem. Lett.* **14**, 8676–8683 (2023).
- Jiao, C., Pei, S., Wu, S., Wang, Z. & Xia, J. Tuning and exploiting interlayer coupling in two-dimensional van der Waals heterostructures. *Rep. Prog. Phys.* **86**, 114503 (2023).
- Fan, D., Xu, J., Ma, M., Liu, J. & Xie, H. P–V–T equation of state of molybdenite (MoS<sub>2</sub>) by a diamond anvil cell and in situ synchrotron angle-dispersive X-ray diffraction. *Phys. B* **451**, 53–57 (2014).
- Yan, Y. et al. Interlayer coupling affected structural stability in ultrathin MoS<sub>2</sub>: an investigation by high pressure Raman spectroscopy. *J. Phys. Chem. C* **120**, 24992–24998 (2016).
- Chen, Y. et al. Pressurizing field-effect transistors of few-layer MoS<sub>2</sub> in a diamond anvil cell. *Nano Lett.* **17**, 194–199 (2017).
- Nayak, A. P. et al. Pressure-dependent optical and vibrational properties of monolayer molybdenum disulfide. *Nano Lett.* **15**, 346–353 (2015).
- Sugai, S. & Ueda, T. High-pressure Raman spectroscopy in the layered materials 2H-MoS<sub>2</sub>, 2H-MoSe<sub>2</sub>, and 2H-MoTe<sub>2</sub>. *Phys. Rev. B* **26**, 6554–6558 (1982).
- Cheng, X. et al. Thickness-dependent phase transition and optical behavior of MoS<sub>2</sub> films under high pressure. *Nano Res* **11**, 855–863 (2018).
- Li, X. et al. Pressure and temperature-dependent Raman spectra of MoS<sub>2</sub> film. *Appl. Phys. Lett.* **109**, 242101 (2016).
- Yang, M. et al. Anharmonicity of monolayer MoS<sub>2</sub>, MoSe<sub>2</sub>, and WSe<sub>2</sub>: a Raman study under high pressure and elevated temperature. *Appl. Phys. Lett.* **110**, 093108 (2017).
- Chi, Z.-H. et al. Pressure-induced metallization of molybdenum disulfide. *Phys. Rev. Lett.* **113**, 036802 (2014).
- Pimenta et al. Pressure tuning of minibands in MoS<sub>2</sub>/WSe<sub>2</sub> heterostructures revealed by moiré phonons. *Nat. Nanotechnol.* **18**, 1147–1153 (2023).
- Verble, J. L. & Wieting, T. J. Lattice mode degeneracy in MoS<sub>2</sub> and other layer compounds. *Phys. Rev. Lett.* **25**, 362–365 (1970).
- Li, H. et al. From bulk to monolayer MoS<sub>2</sub>: evolution of Raman scattering. *Adv. Funct. Mater.* **22**, 1385–1390 (2012).
- Zhang, X. et al. Raman spectroscopy of shear and layer breathing modes in multilayer MoS<sub>2</sub>. *Phys. Rev. B* **87**, 115413 (2013).
- Liang, L. et al. Low-frequency shear and layer-breathing modes in Raman scattering of two-dimensional materials. *ACS Nano* **11**, 11777–11802 (2017).
- Zhao, Y. et al. Interlayer breathing and shear modes in few-trilayer MoS<sub>2</sub> and WSe<sub>2</sub>. *Nano Lett.* **13**, 1007–1015 (2013).
- Klotz, S., Chervin, J. C., Munsch, P. & Le Marchand, G. Hydrostatic limits of 11 pressure transmitting media. *J. Phys. D Appl. Phys.* **42**, 075413 (2009).
- Lin, M.-L. et al. Raman forbidden layer-breathing modes in layered semiconductor materials activated by phonon and optical cavity effects. *Phys. Rev. Lett.* **134**, 096903 (2024).
- Peelaers, H. & Van de Walle, C. G. Elastic constants and pressure-induced effects in MoS<sub>2</sub>. *J. Phys. Chem. C* **118**, 12073–12076 (2014).
- Zhao, L. et al. Probing anisotropic deformation and near-infrared emission tuning in thin-layered InSe crystal under high pressure. *Nano Lett.* **23**, 3493–3500 (2023).

43. Wieting, T. J. Long-wavelength lattice vibrations of MoS<sub>2</sub> and GaSe. *Solid State Commun.* **12**, 931–935 (1973).
  44. Kresse, G. & Hafner, J. Ab initio molecular dynamics for liquid metals. *Phys. Rev. B* **47**, 558–561 (1993).
  45. Kresse, G. & Furthmüller, J. Efficient iterative schemes for ab initio total-energy calculations using a plane-wave basis set. *Phys. Rev. B* **54**, 11169–11186 (1996).
  46. Kresse, G. & Joubert, D. From ultrasoft pseudopotentials to the projector augmented-wave method. *Phys. Rev. B* **59**, 1758–1775 (1999).
  47. Perdew, J. P., Burke, K. & Ernzerhof, M. Generalized gradient approximation made simple. *Phys. Rev. Lett.* **77**, 3865–3868 (1996).
  48. Monkhorst, H. J. & Pack, J. D. Special points for Brillouin-zone integrations. *Phys. Rev. B* **13**, 5188–5192 (1976).
  49. Grimme, S., Antony, J., Ehrlich, S. & Krieg, H. A consistent and accurate ab initio parametrization of density functional dispersion correction (DFT-D) for the 94 elements H–Pu. *J. Chem. Phys.* **132**, 154104 (2010).
  50. Plimpton, S. Fast parallel algorithms for short-range molecular dynamics. *J. Comput. Phys.* **117**, 1–19 (1995).
  51. Stewart, J. A. & Spearot, D. E. Atomistic simulations of nanoindentation on the basal plane of crystalline molybdenum disulfide (MoS<sub>2</sub>). *Modell. Simul. Mater. Sci. Eng.* **21**, 045003 (2013).
  52. Ouyang, W. et al. Anisotropic interlayer force field for transition metal dichalcogenides: the case of molybdenum disulfide. *J. Chem. Theory Comput.* **17**, 7237–7245 (2021).
  53. Jiang, W. et al. Anisotropic interlayer force field for group-VI transition metal dichalcogenides. *J. Phys. Chem. A* **127**, 9820–9830 (2023).
  54. Parrinello, M. & Rahman, A. Polymorphic transitions in single crystals: a new molecular dynamics method. *J. Appl. Phys.* **52**, 7182–7190 (1981).
- Y.D., J.M. and T.Z. prepared the nanoflake samples and further performed the in situ Raman characterizations and high-pressure experiments. S.L. and X.L. performed the atomistic simulations. J.H. and J.K. performed the DFT calculations and theoretical analyses with J.Z. and G.D. Y.C. and G.D. wrote the manuscript with the essential inputs of all co-authors. All authors have given approval of the final manuscript.

### Competing interests

The authors declare no competing interests.

### Additional information

**Supplementary information** The online version contains supplementary material available at <https://doi.org/10.1038/s41467-025-60211-8>.

**Correspondence** and requests for materials should be addressed to Jun Kang, Xiaoyan Li, Weigao Xu or Yabin Chen.

**Peer review information** *Nature Communications* thanks Konstantinos Papagelis and the other, anonymous, reviewer(s) for their contribution to the peer review of this work. A peer review file is available.

**Reprints and permissions information** is available at <http://www.nature.com/reprints>

**Publisher's note** Springer Nature remains neutral with regard to jurisdictional claims in published maps and institutional affiliations.

**Open Access** This article is licensed under a Creative Commons Attribution-NonCommercial-NoDerivatives 4.0 International License, which permits any non-commercial use, sharing, distribution and reproduction in any medium or format, as long as you give appropriate credit to the original author(s) and the source, provide a link to the Creative Commons licence, and indicate if you modified the licensed material. You do not have permission under this licence to share adapted material derived from this article or parts of it. The images or other third party material in this article are included in the article's Creative Commons licence, unless indicated otherwise in a credit line to the material. If material is not included in the article's Creative Commons licence and your intended use is not permitted by statutory regulation or exceeds the permitted use, you will need to obtain permission directly from the copyright holder. To view a copy of this licence, visit <http://creativecommons.org/licenses/by-nc-nd/4.0/>.

© The Author(s) 2025

### Acknowledgements

This work was financially supported by the National Natural Science Foundation of China (grant numbers 52472040 (Y.C.), 52072032 (Y.C.), 12393831 (J.K.), 12088101 (J.K.), and 12325203 (X.L.)), the 173-JCJQ program (grant No. 2021-JCJQ-JJ-0159 (Y.C.)). W.X. acknowledges the funding support from the National Natural Science Foundation of China (22333004, 22173044), and the Natural Science Foundation of Jiangsu Province (BK20220121).

### Author contributions

Y.C. and W.X. conceived this research project and designed the experiments. G.D. designed and established the ultra-low frequency Raman spectroscopy with the help of L.Z. and S.F. G.D., L.Z., W.H., J.L.,